

Unsteady Aerodynamic Characteristics of Transversely Inclined Prisms Under Forced-Vibration—The Base Intensification Phenomenon

Zengshun Chen

Chongqing University

Jie Bai

Chongqing University

Cruz Y. Li (✉ yliht@connect.ust.hk)

The Hong Kong University of Science and Technology <https://orcid.org/0000-0002-9527-4674>

Yemeng Xu

Chongqing University

Jianmin Hua

Chongqing University

Xuanyi Xue

Chongqing University

Research Article

Keywords: Forced-vibration technique, transversely inclined prisms, unsteady aerodynamics force, aerodynamic damping, response prediction

Posted Date: July 6th, 2021

DOI: <https://doi.org/10.21203/rs.3.rs-609108/v1>

License: © ⓘ This work is licensed under a Creative Commons Attribution 4.0 International License.

[Read Full License](#)

1 **Unsteady Aerodynamic Characteristics of**
2 **Transversely Inclined Prisms under Forced-**
3 **Vibration---The Base Intensification Phenomenon**

4
5 Zengshun Chen ^a, Jie Bai ^a, Cruz Y. Li ^{b,*}, Yemeng Xu ^a, Jianmin Hua ^a, Xuanyi Xue ^{a,*}

6
7 *^a School of Civil Engineering, Chongqing University, Chongqing 400045, China*

8 *^b Department of Civil and Environmental Engineering, The Hong Kong University of Science*
9 *and Technology, Clear Water Bay, Kowloon, Hong Kong, China.*

10
11
12 zchenba@connect.ust.hk (Zengshun Chen); 202016131210t@cqu.edu.cn (Jie Bai);
13 yliht@connect.ust.hk (Cruz Y. Li); xu.ym@cqu.edu.cn (Yemeng Xu); hjm191@163.com (Jiamin
14 Hua); xuexuanyi@126.com (Xue X. Y.)

15
16
17 E-mail address: yliht@connect.ust.hk

18 Mailing address: School of Civil Engineering, Chongqing University, Chongqing 400045,
19 China

20

* Corresponding Author

21 **Abstract**

22 This work, through a series of forced-vibration wind tunnel experiments, investigates the
23 aerodynamic characteristics of square prisms subject to the transverse inclination. An
24 aeroelastic prism was tested under different wind speeds, inclination angles, and oscillation
25 amplitudes. Through analysis on the mean pressure distribution, local force coefficient, force
26 spectra, and aerodynamic damping coefficient, the unsteady aerodynamic characteristics of the
27 configuration were revealed. Empirical observations discovered the *Base Intensification*
28 phenomenon, which refers to a fundamental change in the structure's aerodynamic behaviors
29 given any degrees of transverse inclination. Specifically, it is the intensification of the
30 aerodynamic loading, vortical activities, and aerodynamic damping on only the lower portion
31 of an inclined structure. The phenomenon, being almost impactless to the upper portion, is also
32 insensitive to changes in inclination angle and tip amplitude once triggered by the initial
33 inclination. Analysis also revealed that the origin of Base Intensification phenomenon traces
34 back to fix-end three-dimensional effects like the horseshoe vortex, instead of the
35 predominant Bérnard-Kármán vortex shedding. Moreover, results showed that wind speed is
36 the decisive factor for the structure's crosswind motions. Inside the lock-in region, structure
37 loadings, vortical activities, and the effects of *Base Intensification* are significantly amplified.
38 Beyond the range, the configuration gradually resorts to a quasi-steady linearity. Finally, results
39 from the force-vibration tests were used for the prediction of structure response. Experimental
40 comparison revealed that the predictions notably outperform those based on rigid tests,
41 forecasting the actual responses with a markedly improved accuracy.

42

43 **Keywords**

44 *Forced-vibration technique; transversely inclined prisms; unsteady aerodynamics force;*
45 *aerodynamic damping; response prediction.*

46

47

48 **Highlights:**

49 ✓ A series of forced-vibration tests were performed to obtain unsteady aerodynamic forces
50 acting on a transversely inclined slender prism.

51 ✓ The nonlinear, unsteady aerodynamics characteristics of transverse inclination have been
52 analyzed.

53 ✓ The *Base Intensification* unsteady phenomenon, which is unique to the transverse
54 inclination, has been identified and introduced.

55 ✓ The response of the prisms predicted by the unsteady aerodynamic forces; the newly
56 proposed prediction method outperforms the traditional method based on rigid tests.

57

58 **1. Introduction**

59 With the continuous improvement of construction technology, modern buildings are becoming
60 increasingly slender and flexible all over the world. Consequently, the influence of wind
61 loading and wind-induced vibration on super-tall buildings are of great safety concern,
62 particularly after being reminded by the recent vibration of the SEG Tower in Shenzhen.
63 Therefore, studies on the aerodynamic characteristics of super-tall buildings bear critical
64 importance. To date, much remain unexplored for the even the most canonical configurations,
65 for example the square prism. To tackle the outstanding issues, the deepening of our
66 understanding of bluff-body aerodynamics demands persistent effort.

67

68 The aerodynamic characteristic of a structure is the key determinant to its wind-induced
69 response. In the event of excessive excitations, whether by the Vortex-Induced-Vibration
70 (VIV), galloping, or fluttering, irreversible damage may be incurred on the structure. In many
71 cases, the modes of vibration are closely associated to the aerodynamic damping, because a
72 negative aerodynamic damping will aggravate the vibration until plastic deformation.
73 Therefore, a series of experimental research have been performed on the aerodynamic
74 characteristics of bluff-bodies. Tanaka *et al.* [1] studied the aerodynamic characteristics of
75 unconventional building models (spiral, cone, *etc.*) through rigid pressure test. Hui *et al.* [2]
76 examined the influence of different façade appendages on the aerodynamic characteristics of
77 high-rise buildings. Likewise, Carassale *et al.* [3] studied the influence of round corners on the
78 aerodynamic characteristics of rectangular prisms. However, these studies are limited to the

79 scenarios when the structure is aligned vertically perpendicular to the incoming flow, which
80 might not be the case for many modern designs of infrastructure. To this end, Hu *et al.* [4]
81 studied the longitudinally inclined (forward and backward) rectangular prism through a series
82 of wind tunnel tests. They concluded that the inclination angle has profound impacts on the
83 aerodynamic characteristics of prisms, yet the degrees of the impact are significantly different
84 depending on the inclination angle. Perhaps the biggest limitation to this work is the rigidity of
85 the test model. Due to the complex behaviors of the fluid and its mutually reinforcing
86 interactive mechanisms with the structure, it is difficult to evaluate the unsteady aerodynamic
87 forces accurately using a rigid model. Aeroelasticity must be included to accommodate the
88 fluid-structure interaction.

89

90 Subsequently, Hu *et al.* [5] confirmed the quasi-static theory inadequate for predicting inclined
91 structural responses using an aeroelastic model. Mannini *et al.* [6] too disproved the theory for
92 low mass-damping structures. Later, Chen *et al.* [7] discovered the *Partial Reattachment*
93 phenomenon for aeroelastic tapered prisms, in which the closure of a separation envelope to a
94 separation bubble by increasing the wind attack angle suppresses the Bérnard-Kármán vortex
95 shedding altogether. Indeed, the quasi-static theory also failed in the prediction of tapered
96 prisms. Research showed that structures with shape irregularities generally disobey the quasi-
97 static theory. The fundamental cause is the neglect of the unsteady effects, which is only
98 captured by aeroelastic measurement. In other word, ignoring the unsteady effects brought
99 about by aeroelasticity is equivalent to a quasi-static prediction, which is bound to deviate from
100 reality.

101

102 To this end, previous research proved that the forced-vibration method produce relatively
103 accurate evaluations of the unsteady effects [8–10]. Kim *et al.* [11] examined the impact of
104 vibration amplitude on the aerodynamic forcing of a structure, finding notable improvements
105 by forced-vibration compared to the rigid test. Furthermore, Chen *et al.* [12, 13] systematically
106 compared the aerodynamic forces measured from rigid, forced-vibration and the hybrid
107 aeroelastic-pressure balance (HAPB) test (*i.e.*, free-vibration). Their analysis showed that the
108 HAPB, being the optimal testing method among the three, accurately depicts the bi-directional
109 feedback loop of the fluid-structure coupling, whereas this loop is utterly absent for the rigid
110 test and unidirectional for the forced-vibration test.

111

112 In addition, Chen *et al.* [14] studied the unsteady aerodynamic forces acting on a rectangular
113 prism using the forced-vibration method, finding that the permission of vibration significantly
114 alters the aerodynamic force coefficient in the crosswind direction, while only minimally
115 affecting those in the alongwind direction. Interestingly, they also found the generalized and
116 local root-mean-square (RMS) lift increases with oscillation amplitude only at low wind speed
117 and remains relatively constant at high wind speed. Furthermore, based on [4] and a series of
118 aeroelastic wind tunnel tests, it was shown that both the oscillation amplitude and wind speed
119 are the key factors affecting the aerodynamic damping of longitudinally inclined prisms,
120 especially in the lock-in region [9]. The inclination angle *per se* may also lead to major
121 deviations of the aerodynamic damping from the vertical case.

122

123 The thorough literature review discloses a critical void in bluff-body aerodynamics, that is,
124 there is yet a study on the transversely inclined prism with the aeroelastic effect. Yet the
125 configuration is highly probable given variations of the wind attack angle. Intuitively, the
126 transverse inclination will modify the aerodynamic characteristics of structures and their
127 surrounding flow field. Perhaps the only referential effort was the one that proposed a modified
128 quasi-steady model for transversely inclined prisms [15]. However, the predicted response was
129 only acceptable for the onset of galloping but notably off thereafter. Therefore, the
130 aerodynamic characteristics brought about by transverse inclination, and the feasibility of the
131 quasi-steady theory for this configuration demand further investigation.

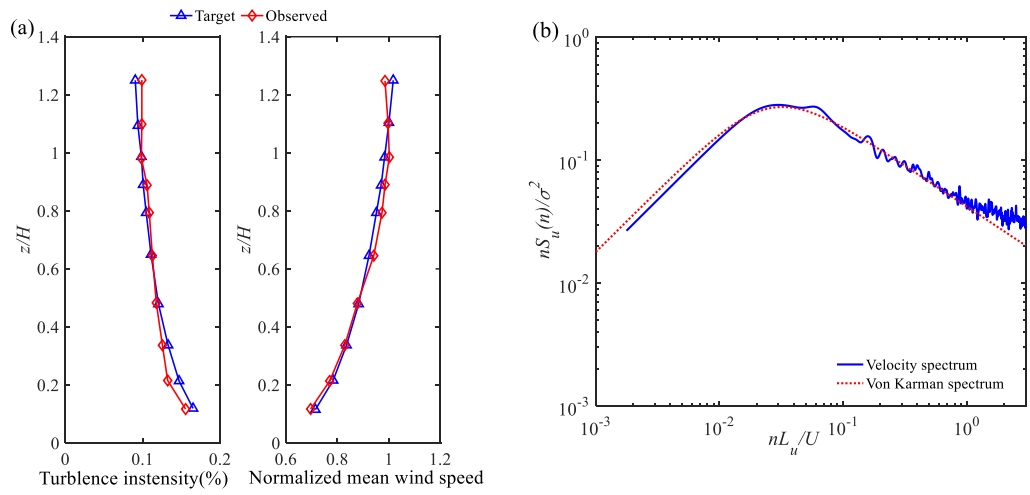
132

133 This work aims to examine the aerodynamic characteristics of transversely inclined prisms.
134 The unsteady aerodynamic forces acting on the model were obtained through a series of forced-
135 vibration tests, and the aerodynamic characteristics of the model were analyzed under
136 representative wind speeds, inclination angles, and vibration amplitude. In composition,
137 Section 1 offers the contextual information and a thorough literature review on the topic of
138 investigation. Section 2 details the methodology of the forced-vibration wind tunnel test.
139 Section 3 presents the identification of the model's aerodynamic characteristics from test
140 results, and elucidates the influence of inclination angle on the aerodynamic characteristics.
141 Section 4 discusses the predicted response of the model by the identified aerodynamic

142 damping, and the comparative observations with the aeroelastic results. Section 5 summarizes

143 the major findings of this work.

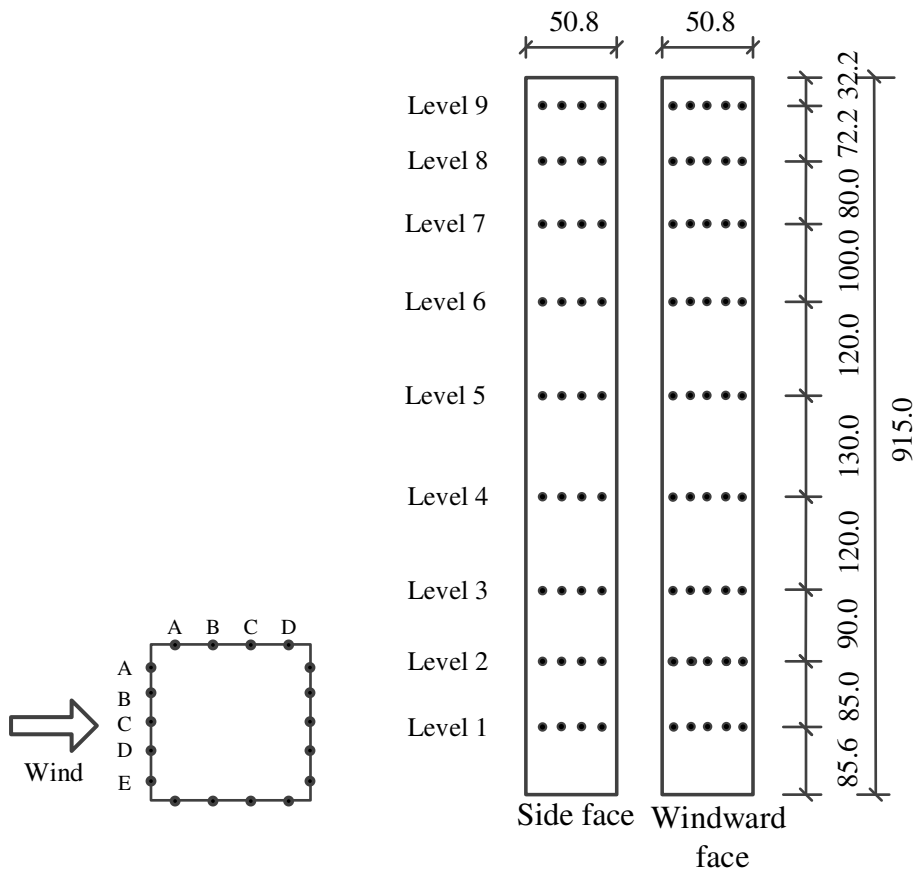
144



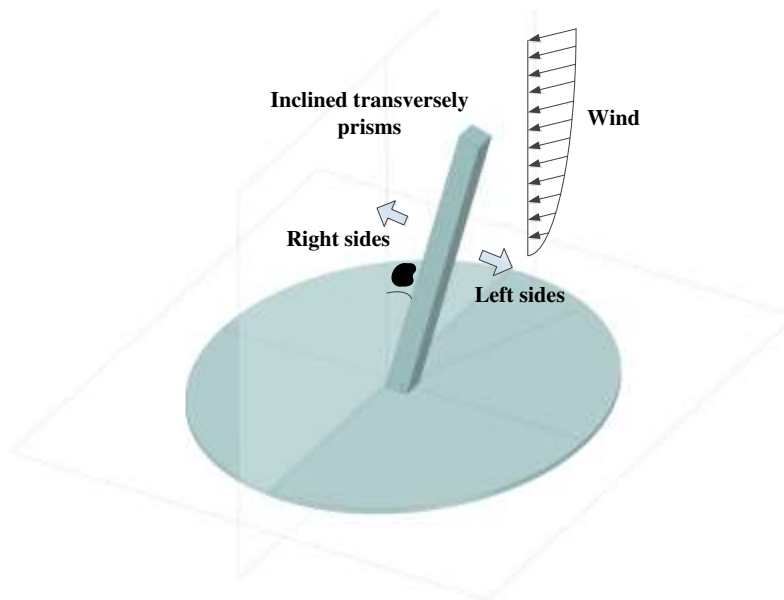
(a) turbulence intensity and wind profile

(b) the wind speed spectrum

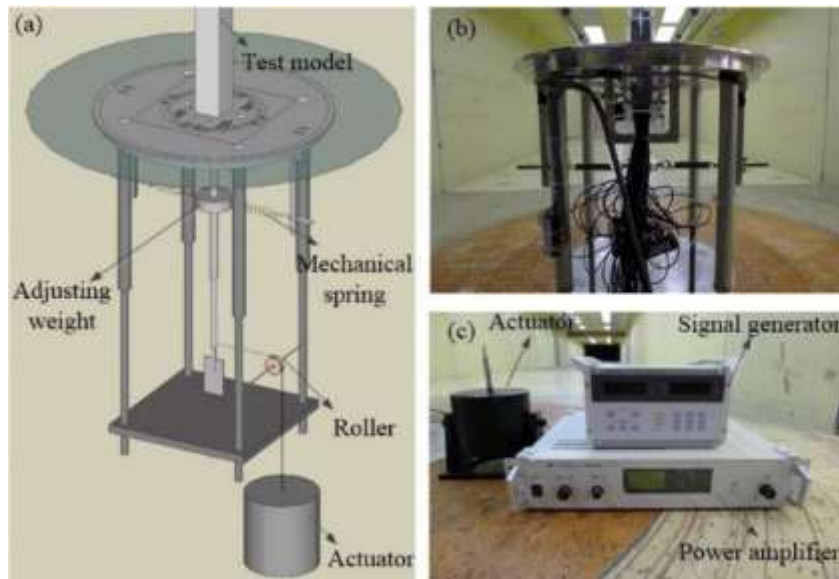
Fig. 1 Wind field characteristics



(a)



(b)



(c)

Fig. 2 Model for pressure measurements: (a) The distribution of Pressure taps; (b) transversely inclined prisms; (c) The forced-vibration device and system

146 The main investigative method of this work is wind tunnel experiment, which proved one of
 147 the most effective method for endeavors in bluff-body aerodynamics. The wind tunnel tests
 148 were performed in the high-speed section of the CLP Power Wind/Wave Tunnel Facility at the
 149 Hong Kong University of Science and Technology. The dimension of the wind tunnel was 29.2
 150 m (Length) \times 3 m (Width) \times 2 m (Height). The corresponding the blockage ratio was 0.78%,
 151 with which undesired influence of tunnel walls on the wind field can be avoided [16]. The
 152 mean wind profile exponent β was determined as 0.15, and the turbulence intensity at the
 153 model top was 10%. The corresponding provisions in the specification were compared with the
 154 wind characteristics measured in this test, as shown in **Fig. 1** (a) and (b). The comparison
 155 shows that the simulated wind characteristics closely replicate the target ones, therefore are
 156 appropriate for wind tunnel testing.

158 **Table 1** Basic parameters of the model and wind tunnel test

| Height (mm) | Pressure Taps | β | Prism Length (mm) | Reduced Wind speeds | Oscillation Amplitude(%) | Inclination Angle α (°) |
|-------------|---------------|---------|-------------------|--|------------------------------|--------------------------------|
| 915 | 162 | 0.15 | 50.8 | 6, 7, 8, 8.5, 9, 9.5, 10, 10.5, 11, 11.5, 12, 13, 14, 15, 16, 18, 20 | 0, 8, 10, 12, 14, 16, 18, 20 | 0, 5, 10, 15, 20, 30 |

159 The test model was a square prism with the dimension 50.8 mm (B) \times 50.8 mm (D) \times 915 mm(H),
 160 where B and D were the length and width of the cross-section and H was the height (**Fig. 2**).
 161 The aspect ratio of the model was 18:1. The natural vibration frequency of the model was set
 162 to 7.8 Hz. In the forced-vibration test, a device installed under the base of the model initiated
 163 harmonic excitations. The inclination angle α of the model varied from 0° to 30°, and the
 164 amplitudes of oscillation was prescribed to be between 6% and 20%.

165
 166 Reduce wind speed $V_r = U/fD_c$ (U is the wind speed at the top of the model, f is the natural
 167 frequency, and D_c is the characteristic length) was determined to be between 6 and 20. More
 168 experimental details are summarized in **Table 1**. The sampling frequency and the duration were
 169 set to 500 Hz and 100s. The tip response of the model was obtained by correcting the raw data
 170 measured from the strain gauge at the model base. The unsteady wind pressure on the model
 171 was measured by a Multi-Point Synchronous Pressure Measurement System (SMPSS). **Fig. 2**
 172 (a) shows the distribution of Pressure Taps. It should be emphasized that the pressure and the
 173 response of the test model were measured synchronously. To avoid literary redundancy, more
 174 details can be found in [9], which adopted the same testing parameters.

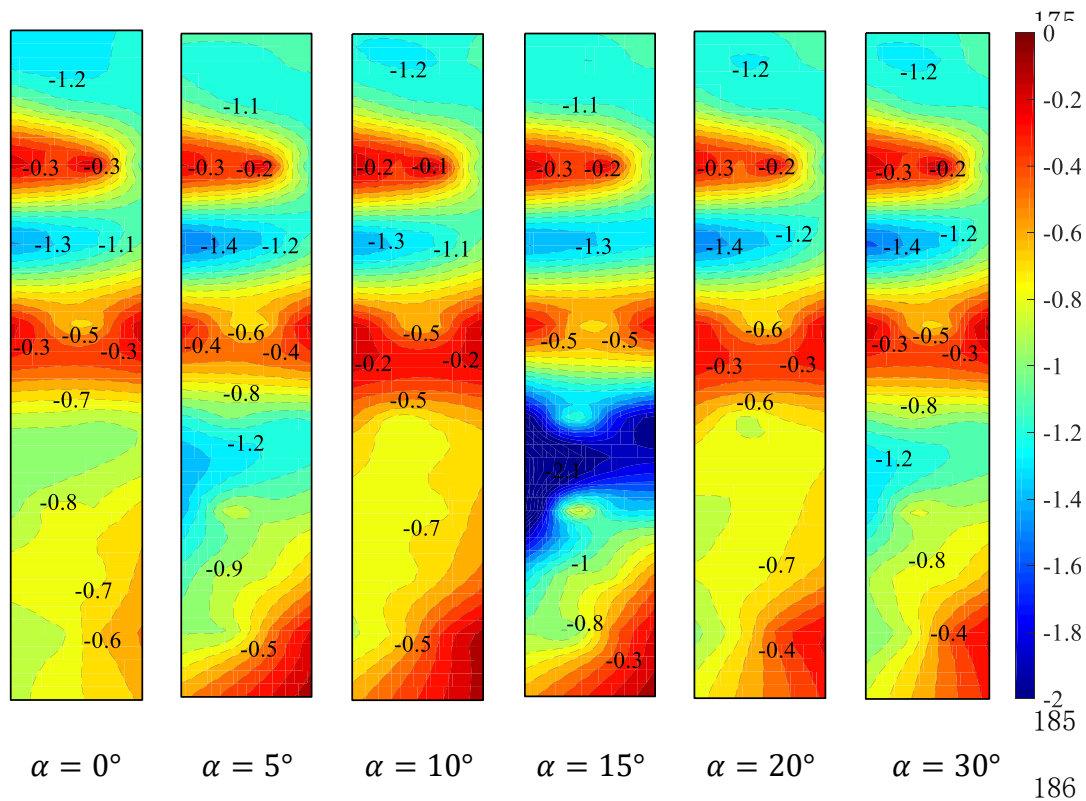


Fig. 3 Mean pressure distribution on the left side ($V_r = 11$)

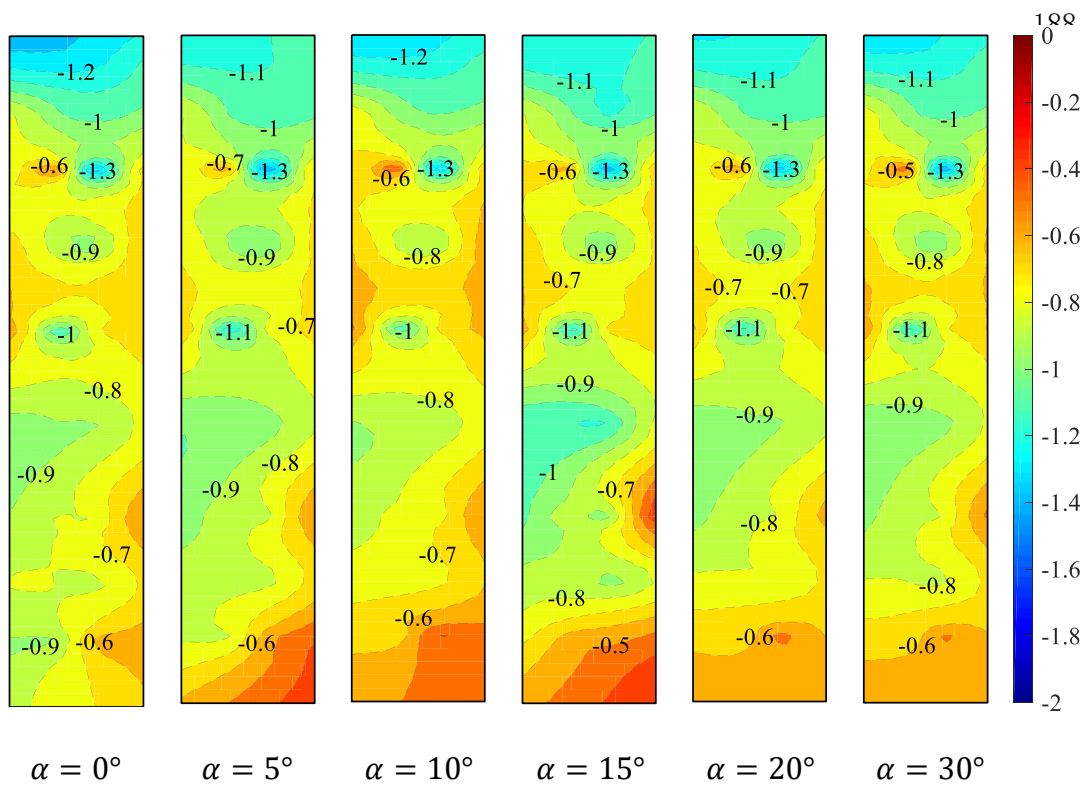


Fig. 4 Mean pressure distribution on the right side ($V_r = 11$)

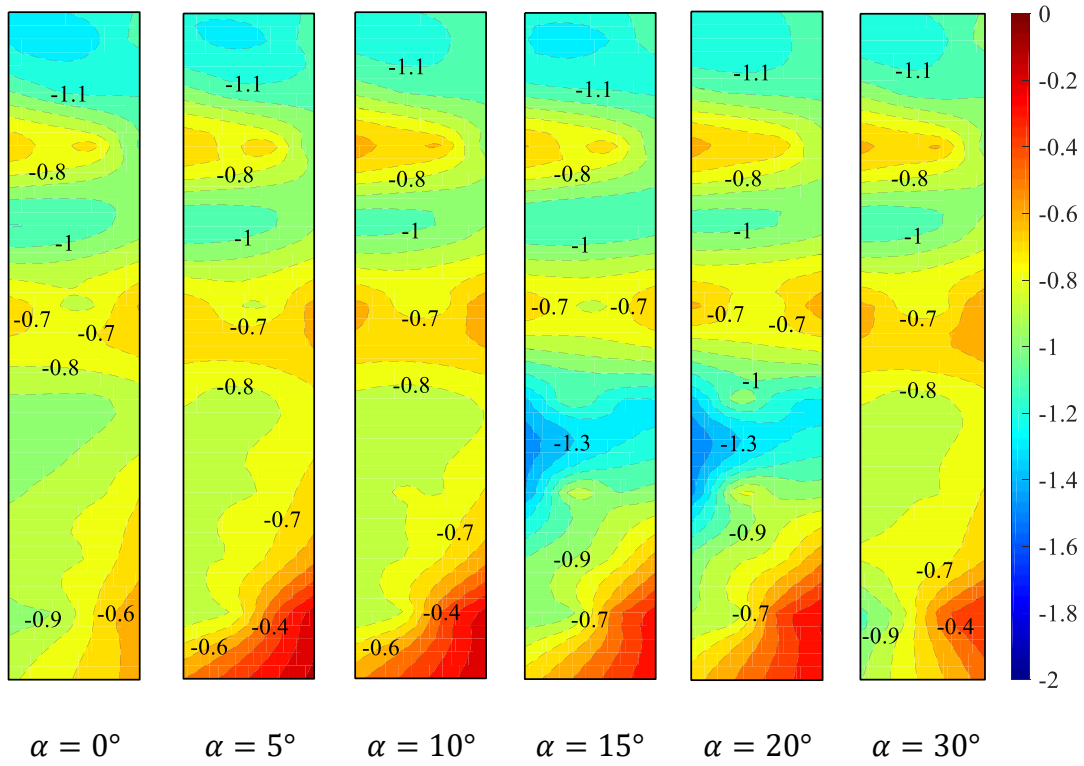


Fig. 5 Mean pressure distribution on the left side ($V_r = 18$)

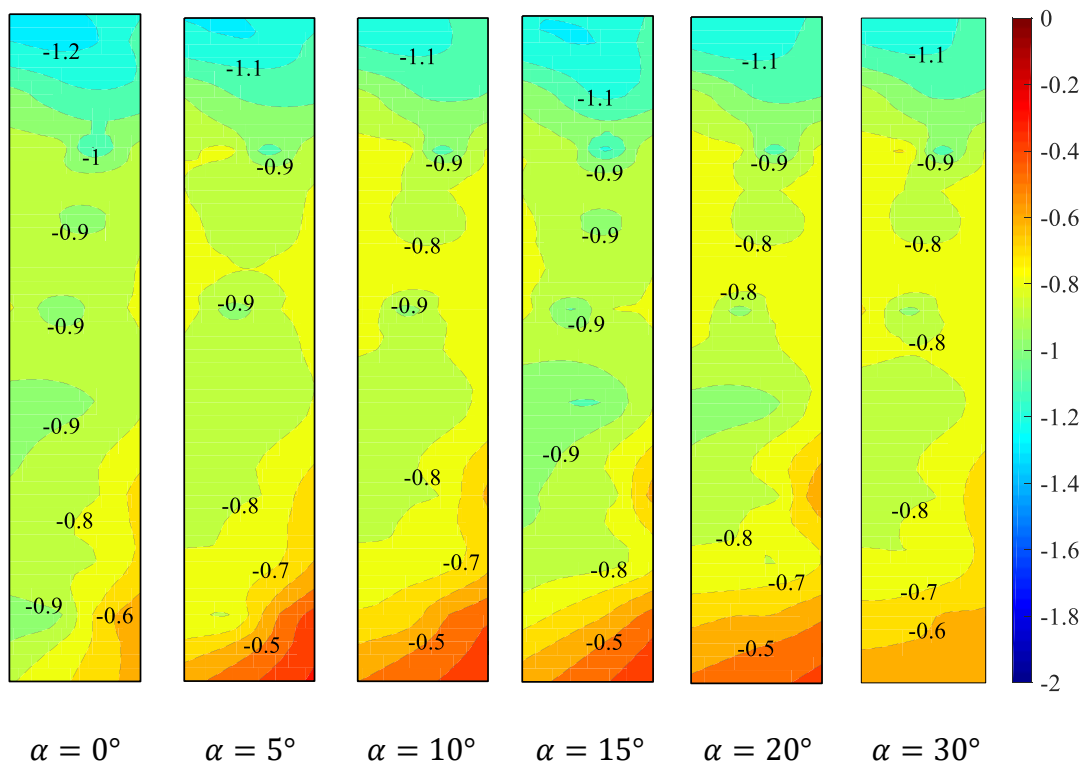


Fig. 6 Mean pressure distribution on the right side ($V_r = 18$)

Fig. 8 Mean pressure distribution on both sides ($V_r = 18$ $\alpha = 10^\circ$)

202 **3.Results and Discussion**

203 **3.1 Unsteady Aerodynamic Coefficient**

204 *3.1.1 Mean Pressure Distribution*

205 Equation (1) was used to calculate the mean wind pressure coefficient C_p acting on the model:

$$C_p = \frac{2P_i}{\rho U^2} \quad (1)$$

206 where P_i is the local pressure acting on the model and ρ is the density of air.

207

208 **Fig. 3-Fig. 8** present the mean pressure distribution of the model surface at different inclination
209 angles α and vibration amplitude σ_y/D . Due to the change of wind attack angle as the result
210 of transverse inclination, the flow separation at the leading edge is not exactly symmetrical.
211 Therefore, perhaps the most representative observations come from pressure distributions on
212 the side faces. Given the abundance of test results, the most insightful sets of data, with wind
213 speeds of $V_r = 11$ and $V_r = 18$ and vibration amplitudes $\sigma_y/D = 0\%$, 8% , and 18% , are
214 presented. $V_r = 11$ is characteristic of the lock-in region and $V_r = 18$ is characteristic of the
215 high wind speed region. It is also important to define the orientation of the side faces for the
216 convenience of subsequent discussion. As shown in **Fig. 2 (b)** , the left side refers to the near-
217 wind side that faces the ground. The right side refers to the far-wind side that faces the ceiling.

218

219 In the most general sense, the side faces of the model experiences suction (negative pressure).

220 The sharpness of pressure gradients seems to be inversely proportional to the wind speed,

221 although this might be directly attributed to the lock-in effect. In addition, the pressure
222 distribution on either faces are completely different, where dynamical activities on the left face
223 are of greater intensity and subject to more prominent changes with α . Moreover, the lower
224 half of the model is greatly affected by α , whereas the upper half remains relatively insensitive.

225

226 Specifically, we examine the side faces in parallel for better comparisons. **Fig. 3** and **Fig. 4**
227 show the wind pressure distribution of the left and right faces of different α at velocity $V_r =$
228 11, and no forced-vibration $\sigma_y/D = 0\%$. On the right side, α has limited influence on the
229 pressure of the top half of the model. However, the model base is quite sensitive to α : low
230 suction zones propagate from the rear corner of the model base towards higher level, before
231 being thwarted near the mid-span. In this lock-in region, α promotes the restoration of pressure
232 most prominently at 15° . In addition, the maximum pressure on the right side is $C_p = -1.3$ at
233 the Level 8, which stays fairly consistent at all α 's.

234

235 In comparison to that of the right side, the pressure distribution on the left side is more
236 sophisticated. First, the top half of the model remains unaffected by α , but a region of sharp
237 pressure restoration ($C_p = -0.2$ and -0.3) persists at about $1/5H$ from the free-end. The
238 location corresponds precisely with that of the maximum pressure on the right side. At the
239 model mid-span, a sharp band of high-pressure zone runs across the entire model width, which
240 is consistently maintained with only slight alterations at $\alpha = 10^\circ$ and 15° . Conversely, the
241 bottom half of the model is subjected to substantial variations. A pressure restoration zone near

242 the rear end of the base is evident. The restoration is accompanied by a sharply propagating
243 pressure gradient. Yet, perhaps the most drastic and unexpected change occurs at $\alpha=15^\circ$. A
244 region of extreme suction, at $C_p = -2.1$, occurs just below the mid-span high-pressure band.
245 Just below this suction zone, another sharp pressure gradient takes place and restores pressure
246 back to as high as $C_p = -0.3$. From an aerodynamics point-of-view, the logical explanation
247 is that at $\alpha = 15^\circ$, an intense separation bubble forms, which is associated to reattachment and
248 the impingement of certain types of vortices. However, the affiliation of these vortices requires
249 further evidence.

250

251 With the increase of wind speed (**Fig. 5** and **Fig. 6**) beyond the lock-in region to $V_r = 18$, the
252 most visible change is the moderation of extremities in the pressure distribution on either side.
253 Evidently, the pressure patterns for the right side resembles those of the lock-in case, except
254 displaying less variability and milder extreme values. For example, the observed maxima
255 reduced from -1.3 to -1.0. On the left side, similar observations are made. Features like the
256 leading-edge restoration near the free-end, mid-span restoration band, and the suction zone all
257 appear with much milder intensity. Interestingly, near the model base, the pattern and intensity
258 of the pressure distribution are almost identical between $V_r = 11$ and 18. This is to say,
259 knowing the lock-in is excited by the resonance between the Karman vortex and structure
260 motion, the vortical activities on the model base are not associated with the Bérnard-Kármán
261 vortex shedding. Instead, they are perhaps associated with the horse-shoe vortex that occurs
262 universally near the base of three-dimensional bluff-bodies.

263

264 Next, to elucidate the influence of vibration amplitude on wind pressure distribution, **Fig. 7**
265 and **Fig. 8** present a comparison of the mean wind pressure distribution at $\alpha = 10^\circ$, wind speed
266 at $V_r = 11$ and $V_r = 18$, and amplitude at 0%, 8% and 18%. Clearly, pressure distribution is
267 only almost insensitive to the vibration amplitude. Although minute variations can be observed,
268 but when compared to the degree of change in vibration amplitude (*i.e.*, from 0-18%), such
269 differences are trivial.

270

271 **3.1.2 RMS Generalized Force Coefficient**

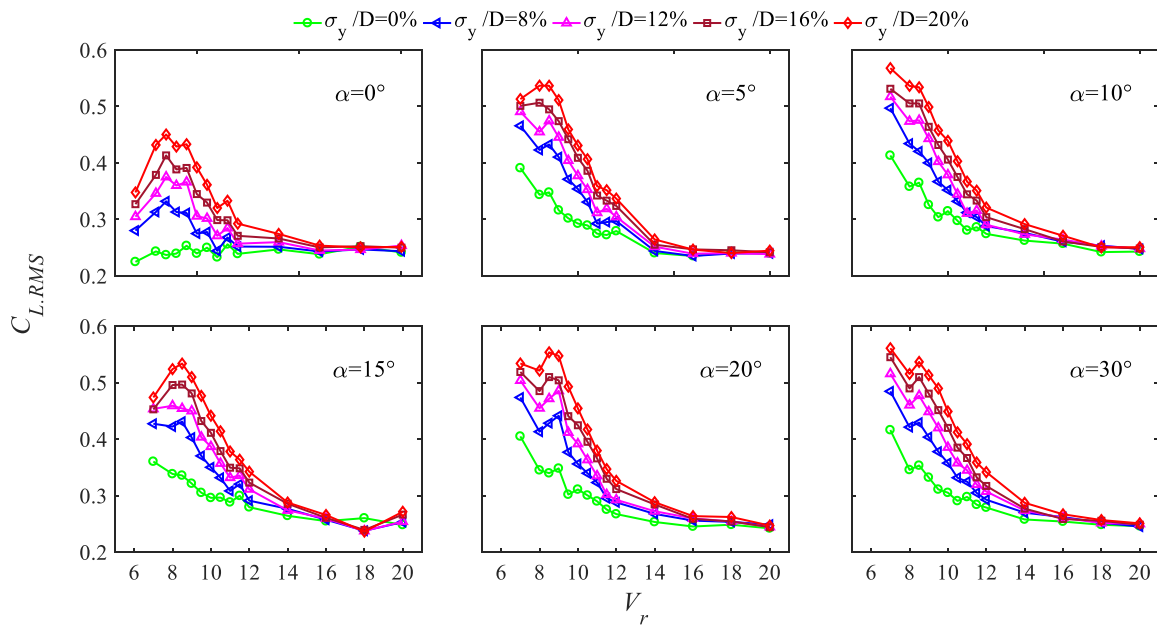


Fig. 9 Generalized RMS force coefficients

272 The unsteady aerodynamic force coefficient in the crosswind direction can be obtained as:

$$\tilde{C}_{L,rms}(z) = \frac{2\tilde{F}_L(z)}{\rho A(z)U^2} \quad (2)$$

$$\tilde{C}_{L,rms} = \frac{\int_0^H A(z)\tilde{C}_L(z)\phi(z)dz}{DH} \quad (3)$$

273 where $\tilde{C}_{L,rms}(z)$ is local RMS force coefficient and $\tilde{F}_L(z)$ is RMS lift force. Equation (3) is
 274 obtained by integrating Equation (2) along the model height, in which $A(z)$ is the local area
 275 at height z , $\phi(z)$ is the function of the first mode, namely $\phi(z) = z/H$.

276

277 Since the mean lift coefficient is approximately zero, only the RMS lift force coefficient bears
 278 significant implications [17]. **Fig. 9** presents the variation of the generalized RMS lift
 279 coefficient at different α , wind speeds and vibration amplitudes. The significant influences of
 280 α and vibration amplitude on the RMS lift are limited to the low-speed range, as all variations
 281 collapse into a single curve around 0.25 after $V_r = 16$. This observation supports the quasi-
 282 steady notion at sufficiently high wind speeds. On the other hand, the proportionality between
 283 the RMS lift and vibration amplitude is uniform for all α , where the self-similar curves are
 284 simply shifted vertically in the low-speed range. Reminded by the observations on the mean
 285 pressure, from which no obvious dependence on vibration amplitude could be deduced, it is
 286 concluded that the primary effect of the vibration amplitude is projected onto the RMS force.
 287 This is to say, increasing the vibration amplitude enhances the turbulence activities of the
 288 surrounding field, so that the intensified fluctuating wind field transfers the added turbulent

289 kinetic energy (TKE) onto the structure as fluctuating pressure. The extra TKE is attributed to
290 the added kinetic energy from the enlarged vibration amplitude and reflects this intensification
291 of the unsteady effects.

292

293 With a rather straightforward proportionality of the vibration amplitude, the effect of α on the
294 RMS lift becomes lucid. First, an increase of α , regardless of the extent, significantly amplifies
295 the RMS lift by at least 20% (some even to 100%). Second, compared to the vertical case ($\alpha =$
296 0°), any alteration of α induces the lock-in effect for the non-vibrating case ($\sigma_y/D = 0\%$).
297 Finally, an increase of α only minimally affect the maximum RMS lift, as its magnitude
298 generally floats around 0.55. All these observations point to a single fact: the aerodynamic
299 characteristics of the configuration experience a sudden change after prescribing an α to the
300 vertical case, but once taken place, further increase of α project minimal impacts.

301

302 *3.1.3 RMS Local Force Coefficient*

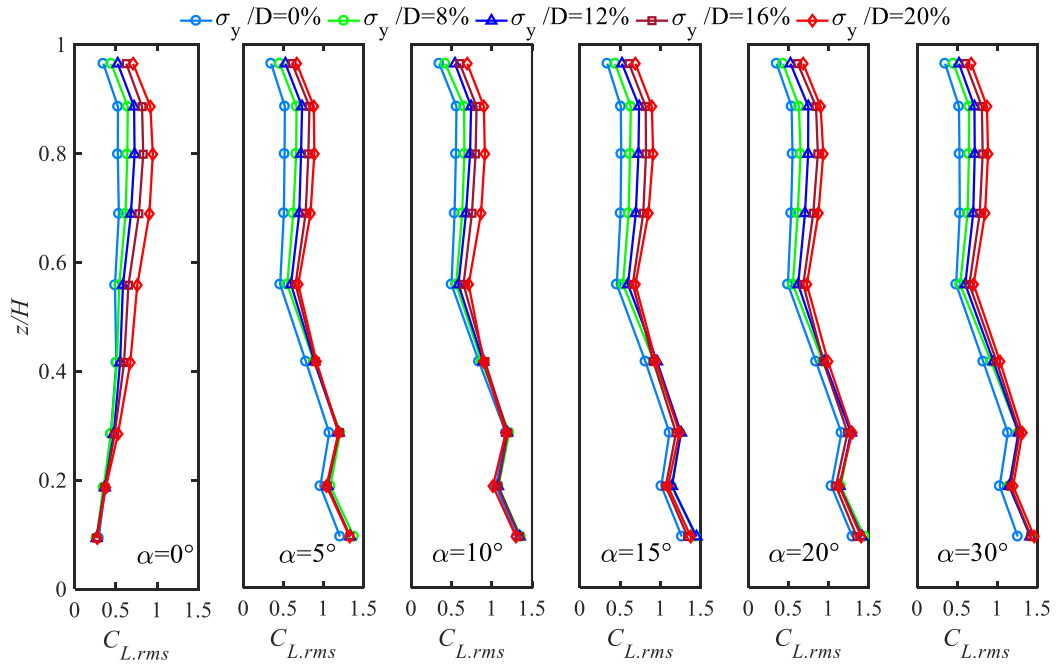


Fig. 10 Local RMS lift coefficient in the low wind speed ($V_r = 11$)

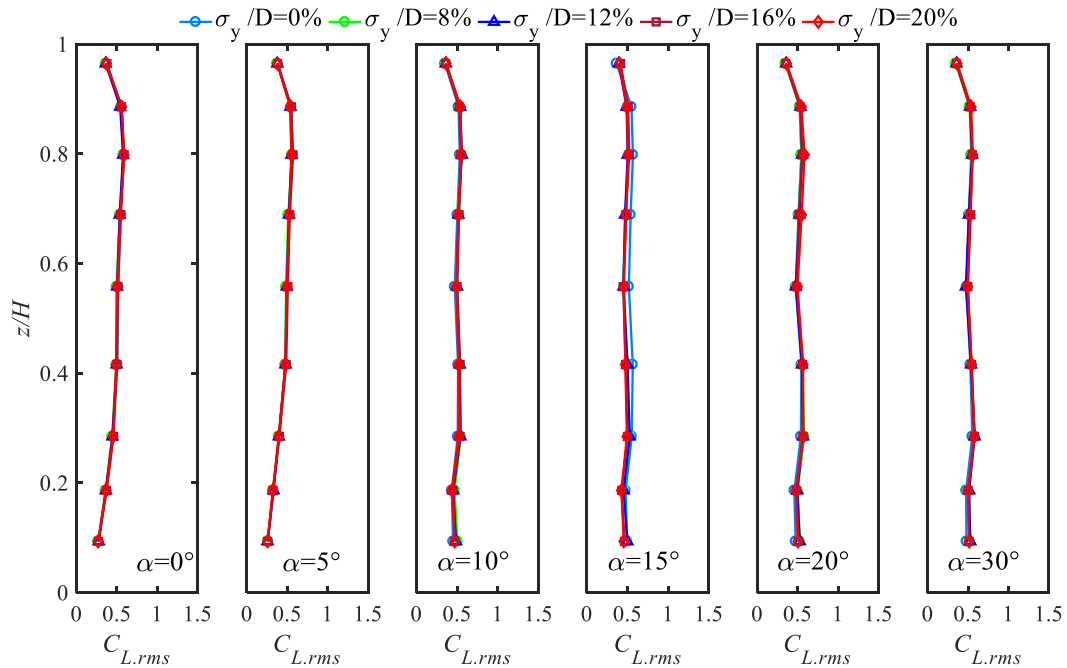


Fig. 11 Local RMS lift coefficient in the high wind speed ($V_r = 18$)

303 To instigate better understanding of the interaction between the structure and fluid, the local

304 RMS lift force coefficients showing the distribution of aerodynamic forces along the model

305 height is calculated by Equation (2). **Fig. 10** and **Fig. 11** present the local RMS lift in the lock-
306 in region ($V_r = 11$) and in the high wind speed ($V_r = 18$) at vibration amplitudes 0%, 8%, 12%,
307 16%, and 20%.

308

309 For the lock-in case (**Fig. 10**), the bi-polar change induced by α is clear. The vertical case
310 differs fundamentally from all other cases. The local RMS lift of the vertical case maximizes
311 at Level 8 ($z/H = 0.8$), whereas those of all other cases maximize at the model base ($z/H=0.1$).
312 In fact, the profiles of all the cases with altered α are self-similar, showing that, after the initial
313 perturbation, a further increase of α does not affect the unsteady forces acting on the model.
314 Furthermore, by close inspection, the profiles can be divided into two halves separated at Level
315 5. A prescription of α only promotes the RMS lift on the bottom half, the lower the more
316 significant. Yet, α minimally, if at all, affects the upper half of the model. This observation
317 echoes with the mean field distribution in **Fig. 3** and **Fig. 4**. By contrast, the vibration amplitude
318 affects only the upper half of the model, as an increase of amplitude instigates a proportional
319 increase in the RMS lift.

320

321 The high-speed case (**Fig. 11**) displays shows the local RMS is generally uniform across the
322 model height and unaffected by either α or vibration amplitude. The collapse of all self-similar
323 curves into a single curve reinforces the quasi-steady notion for this range of wind speeds.
324 Another interesting observation is made on the upper half. On contrary to intuitions, the

325 maximum RMS lift for the upper half does not occur at the free-end but immediately below.

326 This observation bears critical importance and will be discussed in the subsequent sections.

327

328 **3.2 Power Spectral Density**

329 *3.2.1 Generalized Force Spectra*

330 **Fig. 12** and **Fig. 13** present the generalized force spectra in the crosswind direction at $\alpha = 0^\circ$,
331 15° and 30° . The $\sigma_y/D = 0\%$ case represents model with infinite rigidity, which does not
332 consider any fluid-structure interaction. As the result, only one peak [18] corresponding to the
333 frequency of the Bérnard-Kármán vortex shedding is observed. With vibration amplitudes, the
334 forced-vibration tests consider the one-way fluid-structure interaction (*i.e.*, from structure to
335 fluid), thus two peaks appear.

336

337 In the high-wind case (**Fig. 13**), the two peaks are well separated. The peak of lower frequency
338 corresponds to the natural frequency (7.8Hz) of the model. The peak of higher frequency
339 corresponds to the frequency of the Bérnard-Kármán vortex shedding. Evidently, an increase
340 of α , though enhancing the sharpness of the structure frequency, does not change the Karman
341 shedding activity at all. An increase of vibration amplitude only promotes the energy content
342 by slightly widening the peaks.

343

344 The lock-in case (**Fig. 12**), by contrast, is much more complicated. At $V_r = 11$, two
345 frequencies are close to each other, and a clear merging of the peaks is observed. The merging,

346 or the resonance, between the structure and the Bérnard-Kármán vortex shedding frequencies
 347 amplifies the peak amplitude at the reduced frequency of ~ 0.09 . With an increased vibration
 348 amplitude, the second peak becomes increasingly merged into the first peak, while the
 349 frequency of the latter remains unchanged, hence the name *lock-in*. In the $\sigma_y/D = 18\%$ case,
 350 a third peak also appears around 0.18, which is believed to be the second harmonic of the
 351 primary lock-in frequency. Finally, as expected, α has minimal effects on the lock-in behavior.

352

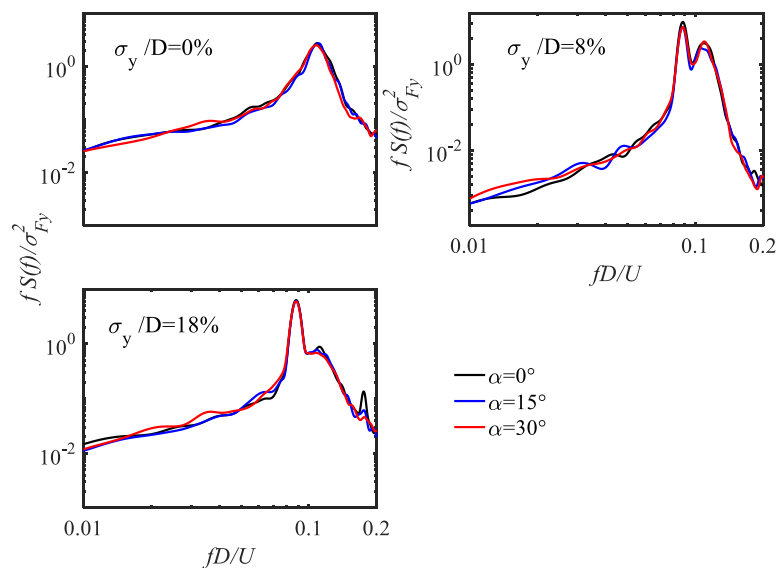


Fig. 12 Generalized force spectrum in the crosswind direction

$$(V_r = 11)$$

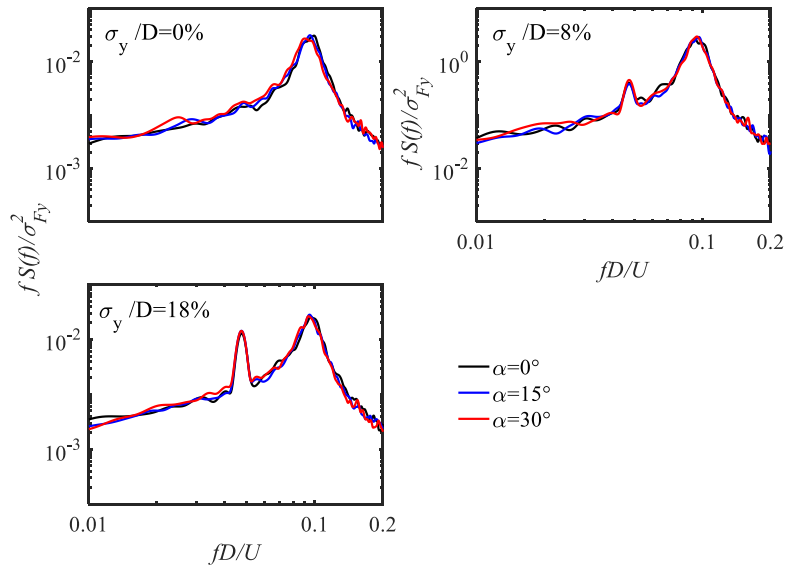
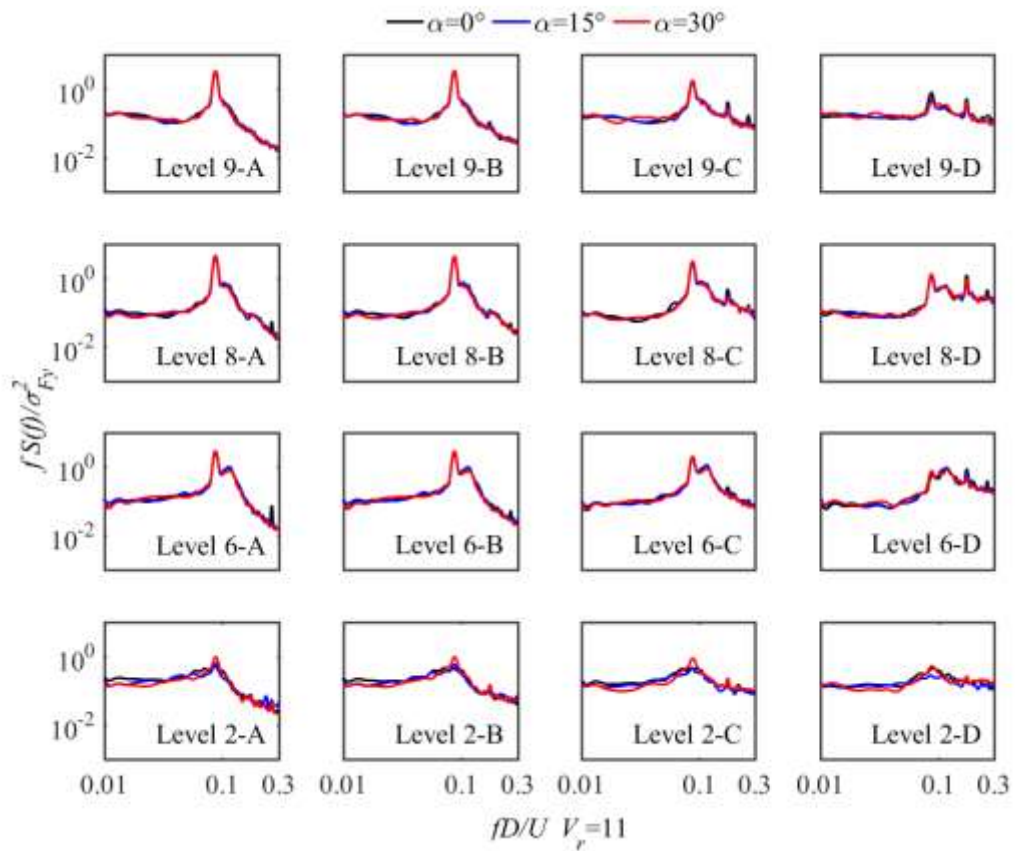


Fig. 13 Generalized force spectrum in the crosswind direction

$$(V_r = 18)$$

354 *Pointwise Pressure Spectra*



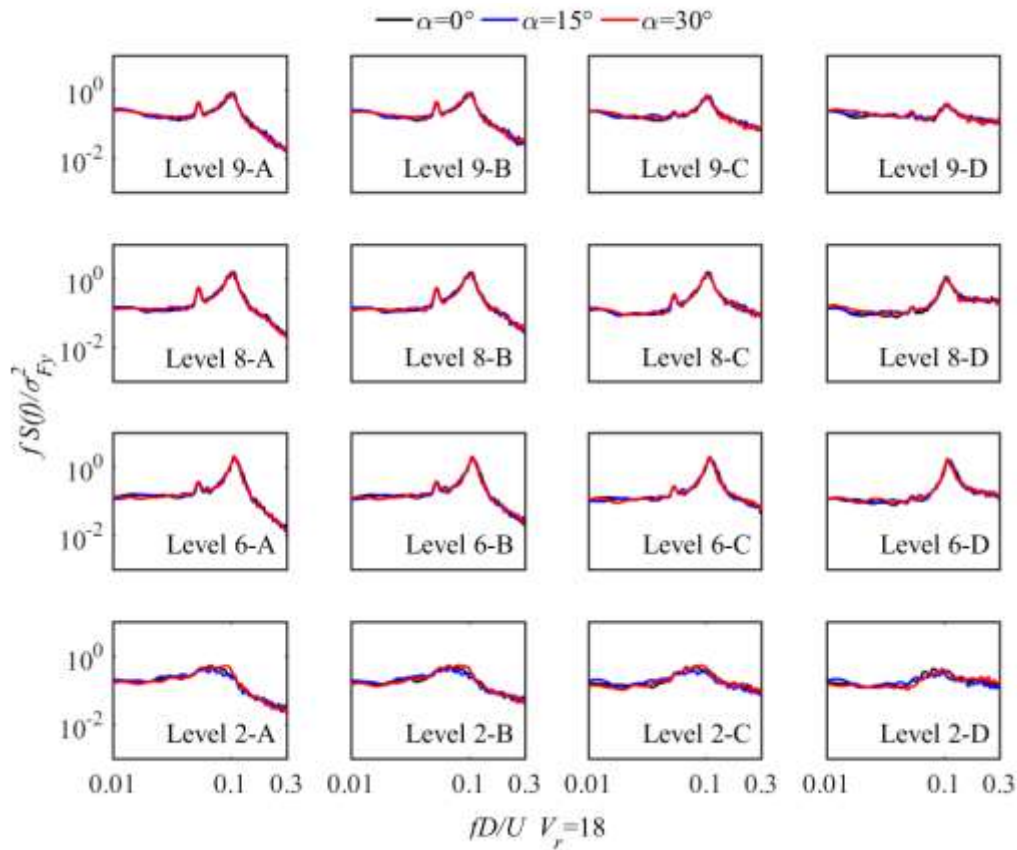


Fig. 14 Spectra of pointwise pressures on the side face of the test model at different

levels: $V_r = 11$ and $V_r = 18$

355 **Fig. 14** presents the pointwise pressure spectra at different altitudes. At the lock-in speed, the
 356 merged main peak becomes increasingly sharp with height, corresponding to the intensifying
 357 vortex shedding activity approaching the free-end. In addition, due to the redistribution of
 358 energy [19, 20], the peak values of downstream of the test model are significantly smaller than
 359 those upstream. However, at the high wind speed, the two peaks are well separated, marking
 360 the disentangled frequencies beyond the lock-in region.

361

362 **Fig. 15** shows the pointwise spectra of point A of the model at different heights in the lock-in
 363 speed ($V_r = 11$), which is at the leading edge of the model. The Karman shedding phenomenon

364 intensifies with height and is insensitive with α except at Level 2. Near the base, a notable
365 proportionality of vortical activity and α is observed. In general, the prominent effects of
366 transverse inclination is limited to the model base where the Karman shedding is heavily
367 disrupted.

368

369 **3.3 Strouhal number**

370 **Fig. 16** shows the altitudinal *Strouhal Number* (St) of the model at high wind speed ($V_r = 18$).

371 The variations of St with α are consistent with previously observed patterns on the mean
372 pressure and RMS lift: the transverse inclination angle affect only the bottom half of the model.

373 In the upper half, St is uniform at 0.11, and it drops to as low as 0.07 near the base. Interestingly,
374 all inclined cases exhibit greater St compared to the vertical case except for $\alpha = 10^\circ$. The
375 changing of St at the base signals a shift in the dominant vortical mechanism, which will be
376 further reinforced by upcoming observations.

377

378 **Fig. 17** presents a comparison of the Karman shedding frequency of the forced-vibration and
379 rigid tests. In the rigid model, the frequency exhibits a linear relationship with wind speed. By
380 contrast, in the forced-vibration test, although the linearity is the same at high wind speeds,
381 fluctuations exist at low speeds. Most notably, inside the lock-in region, the shedding frequency
382 is locked with the natural frequency of the structure (7.8 Hz) for a range of velocities. The
383 platform at 7.8 Hz , after persisting for a range of velocities, is suddenly broken to meet the

384 linearity. This vivid manifestation of the lock-in phenomenon is also evident for all α 's and is
 385 in agreement with previous studies[14, 18, 21].

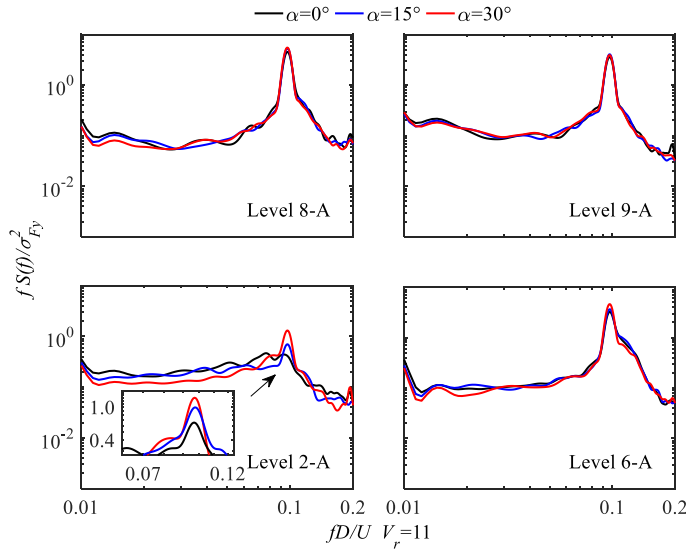


Fig. 15 Pointwise spectra analysis at points A at different heights

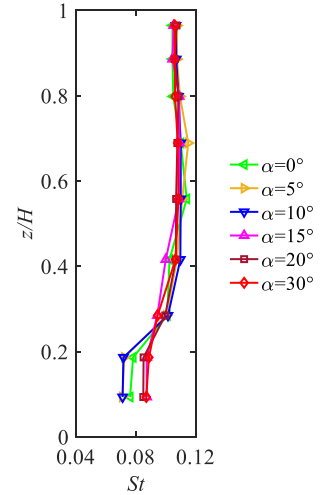


Fig. 16 Local Strouhal numbers ($V_r = 18$)

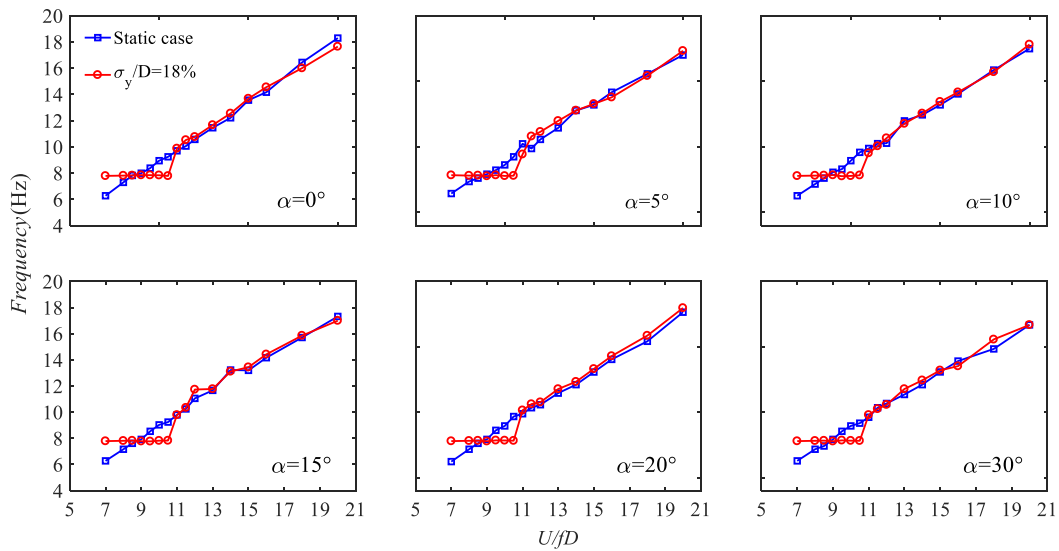


Fig. 17 Comparison of static and forced-vibration tests with vortex shedding frequency

386 **4. Identification of Aerodynamic Damping and Response Prediction**

387 **4.1 Identification of Aerodynamic Damping**

388 Galloping, flutter and Vortex-Induced Vibration (VIV) are main modes of aeroelastic vibration
389 in crosswind direction, and the aerodynamic damping plays a key role in all of them [22–26].
390 Therefore, it is necessary to study the aerodynamic damping of transversely inclined structures.

391

392 The governing equation of motion of a prism in the crosswind direction is expressed as:

$$m(z)\ddot{v}(z, t) + 2m(z)\xi_v\omega_v\dot{v}(z, t) + kv(z, t) = P(z, t) \quad (4)$$

393 where $m(z)$ is the mass per unit height at altitude z , ξ_v is the damping ratio, ω_v is the
394 natural angular frequency, v is the generalized crosswind displacement, and k is the structure
395 stiffness. $P(z, t)$ is the local crosswind force that consists of the aerodynamic and motion-
396 induced (self-excited) components, which can be expressed as:

$$P(z, t) = 0.5\rho U^2[C_M(z, t) + C_L(z, t)]D \quad (5)$$

397 where $C_M(z, t)$ and $C_L(z, t)$ are the local crosswind aerodynamic force and the motion-
398 induced force coefficients at height z , respectively. ρ is the density of air; U is the wind
399 speed at point of reference.

400

401 In the forced-vibration test, the time history tip response can be expressed as $y(t) =$
402 $\hat{y} \cos 2\pi ft$, where \hat{y} is the maximum standard derivation of the tip response. The motion-
403 induced force consists of the aerodynamic stiffness term in phase with displacement and the
404 aerodynamic damping term in phase with velocity. For super tall buildings, the aerodynamic

405 stiffness term is usually small and can be ignored in crosswind direction. Therefore, only the
 406 aerodynamic damping term is of concern [27]. Accordingly, **Eq. 5** can be expressed as:

$$P(z, t) = S_1 \cos 2\pi ft + S_2 \sin 2\pi ft \quad (6)$$

407 where the aerodynamic damping force coefficient S_1 is expressed as:

$$S_1 = \frac{2}{T} \int_0^T P(z, t) \frac{\dot{y}}{2\pi f \hat{y}} dt \quad (7)$$

408 Since

$$\frac{y}{\hat{y}} = \cos 2\pi ft \quad \text{and} \quad \frac{\dot{y}}{\hat{y}} = \sin 2\pi ft \quad (8)$$

409 The local damping force coefficient $\chi(z)$ is

$$\chi(z) = \frac{2S_1}{\rho D U^2} \quad (9)$$

410 The generalized damping force coefficient κ is

$$\kappa = \frac{\int_0^H \mu(z) \phi(z) dz}{H} \quad (10)$$

411 The normalized damping coefficient χ is

$$\chi = \xi_b / \eta = -\frac{3D}{4\hat{y}} \left(\frac{U}{Dw_v} \right)^2 \kappa \quad (11)$$

412 where $\eta = \rho D^2 / m_v$, ξ_b is aerodynamic damping ratio, m_v is the unit mass.

413

414 *4.1.1 Generalized Aerodynamic Damping Coefficient*

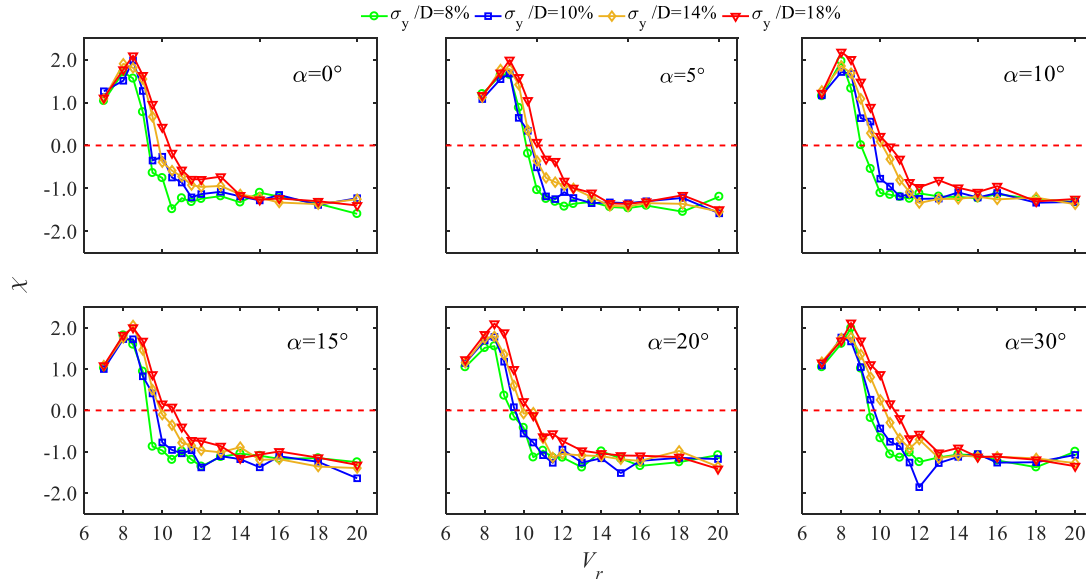


Fig. 18 Generalized aerodynamic damping for transversely inclined prisms

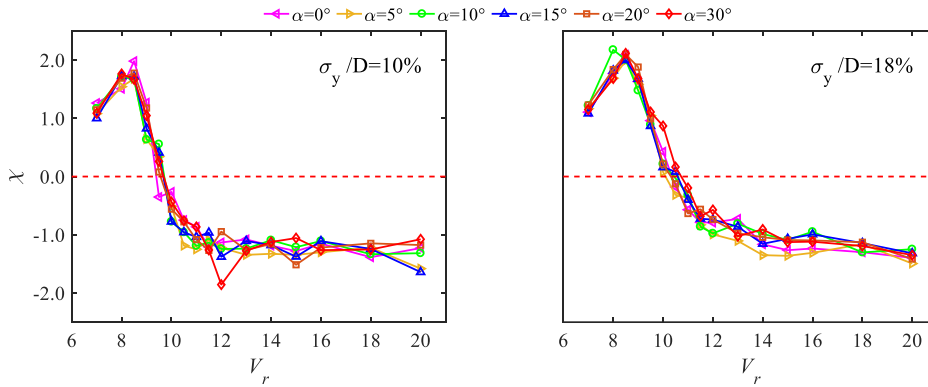


Fig. 19 Comparison of generalized aerodynamic damping at different inclination angles

415 **Fig. 18** presents the generalized aerodynamic damping of the model, which is obtained from
 416 **Eq. (10)** at different vibration amplitude, wind speeds and α . In general, the generalized
 417 aerodynamic damping χ is positive in the lock-in region, while it is negative in the high wind
 418 speeds. The positive aerodynamic coefficient signifies the self-containing nature of the
 419 crosswind vibration. Incidentally, for the zero-ordinate of χ marks the end of the lock-in,
 420 hence prominent vibration. Accordingly, if the aeroelastic effect is ignored (*i.e.*, without

421 aerodynamic damping), there will be over- and underestimations in the predicted response at
422 low and high wind speeds, respectively.

423

424 Both α the vibration amplitude has limited influence on χ , except the latter mildly shifts the
425 corresponding velocity of the zero-ordinate to higher magnitudes. Perhaps the generalized
426 aerodynamic damping force coefficient presented in **Fig. 19** illustrates this insensitivity to a
427 better depiction. The curves of generalized χ are closely self-similar, displaying a lucid message
428 that α and vibration amplitude have minimal influence on χ . In general, wind speed is primary
429 determinant of the behaviors of χ .

430

431 *4.1.2 Local aerodynamic damping coefficients*

432 According to **Eq. (9)**, the local aerodynamic damping of the structure with $\sigma_y/D = 14\%$ is
433 obtained in **Fig. 20**. At sufficiently high levels, the local χ curves resemble those of the
434 generalized χ from **Fig. 19** and **Fig. 20**. Nonetheless, near the model base (Levels 2 and
435 4), $\chi(z)$ is of much less magnitude compared to their high-level counterparts. At Level 2, on
436 contrary to all other cases, $\chi(z)$ barely crosses the zero-ordinate. Perhaps another
437 unexpected observation on the altitudinal effect on $\chi(z)$ is that the maximum local χ does
438 not occur at Level 9, but rather at Levels 7 and 8. Readers are also reminded by similar
439 observations made on the local RMS lift. After consulting fluid mechanics and bluff-body
440 aerodynamics, logical explanations are found for these unintuitive observations.

441

442 The oddities of Level 2 and Level 9 are attributed to different mechanisms either dominating
443 or affecting the aerodynamic behaviors of the structure. As is well-known, the predominant
444 driving mechanism of this configuration, including the excitation of the lock-in phenomenon,
445 is the Bérnard-Kármán vortex shedding. The self-similar local $\chi(z)$ curves, as well as all
446 previous observations, support this notion. The first exception is at the model base. Near the
447 model base, the Bérnard-Kármán vortex shedding is completely overshadowed by fix-end
448 vortical activities like the horse-shoe vortex shedding. As the result, the entire array of
449 aerodynamic parameters at the model base, including the aforementioned mean pressure
450 distribution, RMS lift coefficient, Strouhal number, and aerodynamic damping are
451 fundamentally different from higher levels. As for the other end, the free-end of the model, the
452 Bérnard-Kármán vortex shedding is heavily affected by three-dimensional effects like the
453 downwash axial flow. However, the degree of the influence is not as overwhelming as the
454 horseshoe vortex. Consequently, as reflected by the local RMS lift, local Strouhal number, and
455 here the local aerodynamic coefficient, the Karman shedding maintains its dominance but with
456 a compromised intensity. The maximum local RMS lift and local χ are also recorded slight
457 below the free-end. Nonetheless, and in spite the different driving mechanisms near both ends,
458 the overall lock-in phenomenon dictates the intensity of all aerodynamic activities, thus wind
459 speed becomes the most decisive factor.

460

461 Perhaps this is also a good point to elucidate the aerodynamic effect of the transverse
462 inclination. As all evidence suggest, the transverse inclination induces a bi-polar step-change
463 to the aerodynamic behaviors of the prism. A prescription of any degrees of α projects a notable

464 impact to the bottom half of the model, while the upper half remains unaffected. The impact
 465 consists of drastically enhanced base RMS lift, elevated base Strouhal number, and here the
 466 extended range of positive $\chi(z)$. All of these suggest a universal tenet: the transverse
 467 inclination intensifies fix-end aerodynamic phenomena like the horseshoe vortex, causing a
 468 more erratic wind field near, and stronger loadings onto, the structure base. Yet, once the initial
 469 perturbation, the degree of the intensification is influenced by neither the angle of inclination
 470 nor the amplitude of tip vibration. The practical implications are that structural inclinations of
 471 any orientation, as it easily changes with the wind attack angle, may cause unpredictable wind
 472 environment at the pedestrian level, and demand more safety reinforcement near the build base.
 473 Therefore, in addition to the existing observations in the literature, it is remarked that the *Base*
 474 *Intensification* phenomenon will add another layer of complexity to the aerodynamics of
 475 inclined structures.

476

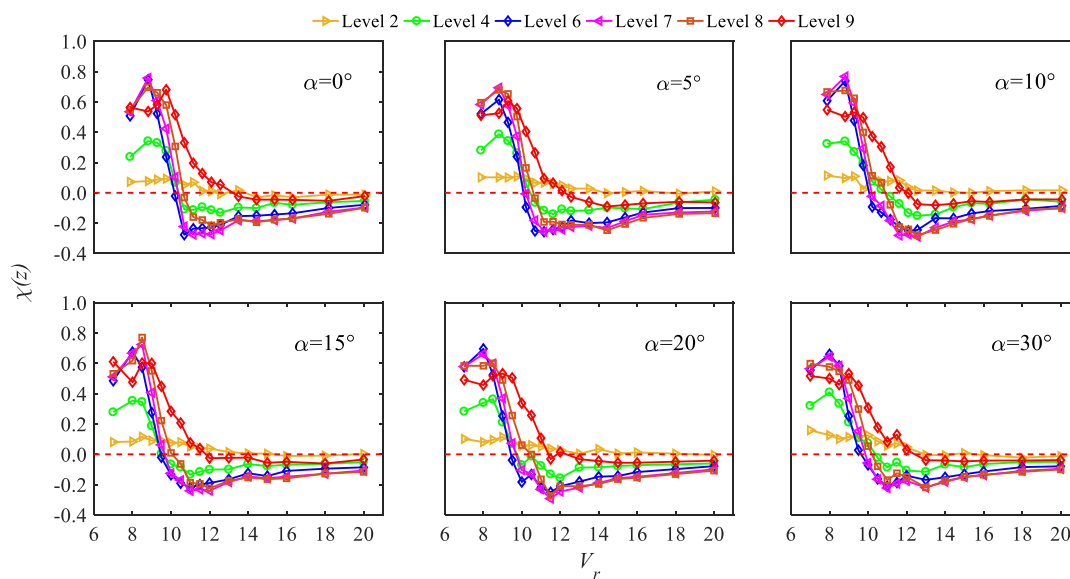


Fig. 20 Local aerodynamic damping for transversely inclined structures

477 **4.2 Response prediction**

478 In this final section, based on the unsteady aerodynamic force obtained from the forced-
479 vibration test, the response of the structure is predicted according to the frequency domain
480 method [12].

$$S_u(w) = S_{Fu}(w) \cdot H^2(w) \quad (12)$$

$$H^2(w) = \{(1 - (f_u/f_s)^2)^2 + 4(\xi_b + \xi_0)^2(f_u/f_s)^2\}^{-1} \quad (13)$$

481 where $S_u(w)$ is the displacement spectrum, $S_{Fu}(w)$ is the force spectrum, $H^2(w)$ is the
482 mechanical admittance, ξ_b is the aerodynamic damping ratio identified by **Eq. (11)**, ξ_0 is the
483 structural damping ratio, and f_s is the natural frequency (7.8Hz).

484

485 The predicted value of the standard tip response is obtained through the integration of **Eq.**

486 (14):

$$\sigma_y = \left\{ \frac{1}{K_s} \int_0^\infty S_u(w) dw \right\}^{1/2} \quad (14)$$

487 where K_s is the model stiffness and σ_y is the tip response.

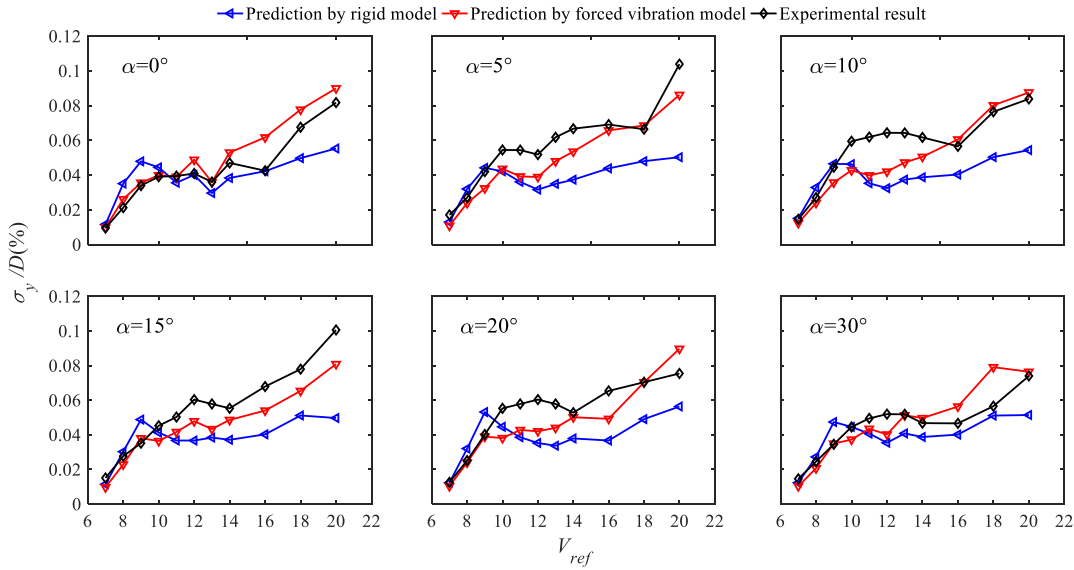


Fig. 21 Comparison between the predicted standard deviation of the test model tip response and the measured values of the aeroelastic test

488 **Fig. 21** shows the comparison between the predicted and measured response at different α 's.
 489 As expected, the predicted responses by forced-vibration and rigid tests increase with wind
 490 speed, generally matching the trend of the experimental result. Nevertheless, notable
 491 differences can be found in the predicted and experimental responses. For the vertical case,
 492 both predictions closely match the measured response, except the forced-vibration response is
 493 almost exact in the lock-in region and overestimates at high wind speeds. Compared to the
 494 underestimating rigid test, the forced-vibration provides more adequate predictions for
 495 structural safety. With inclination, the forced-vibration prediction generally outperforms the
 496 rigid prediction by tallying smaller differences with the experimental value. In specific cases,
 497 such as at $V_r = 20$ and $\alpha = 20^\circ$ and 30° , the forced-vibration prediction outperforms the rigid
 498 one by as much as 28.9% and 27.2%. This is because the rigid prediction completely ignores
 499 the fluid-structure interaction. On this note, even the forced-vibration prediction universally
 500 underestimates the actual response, especially in the lock-in region. The primary cause is that

501 the forced-vibration experiment considers only the one-way fluid-structure interaction by
502 ignoring the flow-induced motion. To provide better predictions, future effort must rely on the
503 results from a free-vibration, fully aeroelastic test.

504

505 **5. Conclusion**

506 In this work, unsteady aerodynamic characteristic of a transversely inclined square prisms were
507 investigated using the forced-vibration technique, in which different wind speeds, inclination
508 angles, and oscillation amplitudes have been tested. Specifically, the configuration's
509 aerodynamic loading, vortical activities, and aerodynamic damping have been analysis.
510 Subsequently, the predicted responses of the forced-vibration and rigid tests were compared
511 with empirical values.

512

513 The central finding of this work is the discovery of the *Base Intensification* phenomenon. It
514 refers to the intensification of the aerodynamic loading, vortical activities, and aerodynamic
515 damping of the lower half of a structure when subjected to transverse inclination. The
516 phenomenon is incurred by any prescription of transverse inclination at any degree. Yet,
517 interestingly, once incurred, it does not intensify nor deteriorate with the angle of inclination
518 and tip vibration amplitude. This bi-polar step-change is associated with the promotion of fix-
519 end effects like the horseshoe vortex shedding. The upper half of the structure, dominated by
520 the Bérnard-Kármán vortex shedding, is generally unaffected by transverse inclination.

521

522 Another major finding is that the wind speed is the most dominant mechanism of the
523 aerodynamic behaviors of the configuration. In the lock-in region, the crosswind vibrations,
524 including the *Base Intensification* phenomenon, are significantly amplified. With a continuous
525 increase of wind speed, the configuration gradually resorts to the quasi-steady linear behavior.

526

527 Based on empirical results, the response of the inclined model is predicted by the force-
528 vibration and rigid test. The force-vibration offers a great improvement to the prediction based
529 on the rigid test. However, since the former only considers the one-way fluid-structure
530 interaction, the prediction still tends to underestimate actual response, particularly inside the
531 lock-in region.

532

533 Finally, some engineering implications and future forecasts deserve a brief discussion. Due to
534 the *Base Intensification* phenomenon, the safety of inclined structures, regardless of inclination
535 orientation, demands more engineering caution. Potential perils like erratic pedestrian-level
536 winds and excessive aerodynamic load on structure base may take place given changes in the
537 wind attack angle. Moreover, future effort shall improve the response prediction by resorting
538 to the free-vibration tests, such that the safety of inclined structures may be better guaranteed
539 in the design stage.

540

541 **Acknowledgement**

542 The work described in this paper was supported by the National Natural Science Foundation
543 of China (Grant No.: 51908090), the Fundamental Research Funds for the Central Universities
544 (Project No.: 2019CDXYTM0032), the Natural Science Foundation of Chongqing, China
545 (Grant No.: cstc2019jcyj-msxm0639, cstc2020jcyj-msxmX0921), the Key project of
546 Technological Innovation and Application Development in Chongqing (Grant No.:
547 cstc2019jscx-gksb0188). The authors appreciate the use of the testing facility, as well as the
548 technical assistance provided by the CLP Power Wind/Wave Tunnel Facility at the Hong Kong
549 University of Science and Technology. The authors would also like to express our sincere
550 thanks to the Design and Manufacturing Services Facility (Electrical and Mechanical
551 Fabrication Unit) of the Hong Kong University of Science and Technology for their help in
552 manufacturing the test rig of the forced vibration wind tunnel test system.

553

554

555 **Declaration**

556 *To be used for all articles, including articles with biological applications*

557

558 **Funding**

559 The work described in this paper was supported by the National Natural Science Foundation
560 of China (Grant No.: 51908090), the Fundamental Research Funds for the Central Universities
561 (Project No.: 2019CDXYTM0032), the Natural Science Foundation of Chongqing, China
562 (Grant No.: cstc2019jcyj-msxm0639, cstc2020jcyj-msxmX0921), the Key project of
563 Technological Innovation and Application Development in Chongqing (Grant No.:
564 cstc2019jscx-gksb0188).

565

566 **Conflict of Interest**

567 The authors declare that they have no conflict of interest.

568

569 **Availability of Data and Material**

570 The datasets generated during and/or analyzed during the current work are restricted by
571 provisions of the funding source but are available from the corresponding author on reasonable
572 request.

573

574 **Code Availability**

575 The custom code used during and/or analyzed during the current work are restricted by
576 provisions of the funding source.

577

578 **Author Contributions**

579 All authors contributed to the study conception and design. Material preparation, data
580 collection and analysis were performed by Zengshun Chen, Jie Bai and Yemeng Xu, Jianmin
581 Hua, and Xuanyi Xue. The first draft of the manuscript was written by Cruz Y. Li and Jie Bai
582 and all authors commented on previous versions of the manuscript. All authors read and
583 approved the final manuscript.

584

585 **Compliance with Ethical Standards**

586 All procedures performed in this work were in accordance with the ethical standards of the
587 institutional and/or national research committee and with the 1964 Helsinki declaration and
588 its later amendments or comparable ethical standards.

589

590 **Consent to Participate**

591 Informed consent was obtained from all individual participants included in the study.

592

593 **Consent for Publication**

594 Publication consent was obtained from all individual participants included in the study.

595 **Reference**

- 596 1. Tanaka, H., Tamura, Y., Ohtake, K., Nakai, M., Chul Kim, Y.: Experimental
597 investigation of aerodynamic forces and wind pressures acting on tall buildings with various
598 unconventional configurations. *J. Wind Eng. Ind. Aerodyn.* 107–108, 179–191 (2012).
599 <https://doi.org/10.1016/j.jweia.2012.04.014>
- 600 2. Hui, Y., Yuan, K., Chen, Z., Yang, Q.: Characteristics of aerodynamic forces on high-
601 rise buildings with various façade appurtenances. *J. Wind Eng. Ind. Aerodyn.* 191, 76–90
602 (2019). <https://doi.org/10.1016/j.jweia.2019.06.002>
- 603 3. Carassale, L., Freda, A., Marrè-Brunenghi, M.: Experimental investigation on the
604 aerodynamic behavior of square cylinders with rounded corners. *J. Fluids Struct.* 44, 195–204
605 (2014). <https://doi.org/10.1016/j.jfluidstructs.2013.10.010>
- 606 4. Hu, Gang, Tse, K.T., Kwok, K.C.S., Chen, Z.S.: Pressure measurements on inclined
607 square prisms. *Wind Struct.* 21, 383–405 (2015).
608 <https://doi.org/10.12989/WAS.2015.21.4.383>
- 609 5. Hu, G., Tse, K.T., Kwok, K.C.S.: Galloping of forward and backward inclined slender
610 square cylinders. *J. Wind Eng. Ind. Aerodyn.* 142, 232–245 (2015).
611 <https://doi.org/10.1016/j.jweia.2015.04.010>
- 612 6. Mannini, C., Marra, A.M., Bartoli, G.: Experimental investigation on VIV-galloping
613 interaction of a rectangular 3:2 cylinder. *Meccanica.* 50, 841–853 (2015).
614 <https://doi.org/10.1007/s11012-014-0025-8>
- 615 7. Chen, Z., Fu, X., Xu, Y., Li, C.Y., Kim, B., Tse, K.T.: A perspective on the
616 aerodynamics and aeroelasticity of tapering: Partial reattachment. *J. Wind Eng. Ind. Aerodyn.*
617 212, 104590 (2021). <https://doi.org/10.1016/j.jweia.2021.104590>
- 618 8. Cooper, K.R., Nakayama, M., Sasaki, Y., Fediw, A.A., Resende-Ide, S., Zan, S.J.:
619 Unsteady aerodynamic force measurements on a super-tall building with a tapered cross
620 section. *J. Wind Eng. Ind. Aerodyn.* 72, 199–212 (1997). [https://doi.org/10.1016/S0167-
621 6105\(97\)00258-4](https://doi.org/10.1016/S0167-6105(97)00258-4)
- 622 9. Chen, Z., Tse, K.T., Kwok, K.C.S., Kareem, A.: Aerodynamic damping of inclined
623 slender prisms. *J. Wind Eng. Ind. Aerodyn.* 177, 79–91 (2018).
624 <https://doi.org/10.1016/j.jweia.2018.04.016>
- 625 10. Zou, L., Li, F., Song, J., Shi, T., Liang, S., Mercan, O.: Investigation of torsional
626 aeroelastic effects on high-rise buildings using forced vibration wind tunnel tests. *J. Wind
627 Eng. Ind. Aerodyn.* 200, 104158 (2020). <https://doi.org/10.1016/j.jweia.2020.104158>
- 628 11. Kim, Y.C., Lo, Y.L., Chang, C.H.: Characteristics of unsteady pressures on slender
629 tall building. *J. Wind Eng. Ind. Aerodyn.* 174, 344–357 (2018).
630 <https://doi.org/10.1016/j.jweia.2018.01.027>

- 631 12. Chen, Z., Huang, H., Tse, K.T., Xu, Y., Li, C.Y.: Characteristics of unsteady
632 aerodynamic forces on an aeroelastic prism: A comparative study. *J. Wind Eng. Ind.*
633 *Aerodyn.* 205, 104325 (2020). <https://doi.org/10.1016/j.jweia.2020.104325>
- 634 13. Chen, Z., Tse, K.T., Kwok, K.C.S., Kareem, A., Kim, B.: Measurement of unsteady
635 aerodynamic force on a galloping prism in a turbulent flow: A hybrid aeroelastic-pressure
636 balance. *J. Fluids Struct.* 102, 103232 (2021).
637 <https://doi.org/10.1016/j.jfluidstructs.2021.103232>
- 638 14. Chen, Z., Tse, K.T., Kwok, K.C.S.: Unsteady pressure measurements on an
639 oscillating slender prism using a forced vibration technique. *J. Wind Eng. Ind. Aerodyn.* 170,
640 81–93 (2017). <https://doi.org/10.1016/j.jweia.2017.08.004>
- 641 15. Chen, Z., Tse, K.T., Hu, G., Kwok, K.C.S.: Experimental and theoretical
642 investigation of galloping of transversely inclined slender prisms. *Nonlinear Dyn.* 91, 1023–
643 1040 (2018). <https://doi.org/10.1007/s11071-017-3926-y>
- 644 16. Holmes, J.D.: *Wind Loading of Structures*. CRC Press (2018)
- 645 17. Lin, N., Letchford, C., Tamura, Y., Liang, B., Nakamura, O.: Characteristics of wind
646 forces acting on tall buildings. *J. Wind Eng. Ind. Aerodyn.* 93, 217–242 (2005).
647 <https://doi.org/10.1016/j.jweia.2004.12.001>
- 648 18. Bearman, P.W., Obasaju, E.D.: An experimental study of pressure fluctuations on
649 fixed and oscillating square-section cylinders. *J. Fluid Mech.* 119, 297–321 (1982).
650 <https://doi.org/10.1017/S0022112082001360>
- 651 19. Kareem, A.: Measurements of pressure and force fields on building models in
652 simulated atmospheric flows. *Sixth US Natl. Conf. Wind Eng.* 36, 589–599 (1990).
653 [https://doi.org/10.1016/0167-6105\(90\)90341-9](https://doi.org/10.1016/0167-6105(90)90341-9)
- 654 20. Kareem, A., Cermak, J.E.: Pressure fluctuations on a square building model in
655 boundary-layer flows. *J. Wind Eng. Ind. Aerodyn.* 16, 17–41 (1984).
656 [https://doi.org/10.1016/0167-6105\(84\)90047-3](https://doi.org/10.1016/0167-6105(84)90047-3)
- 657 21. Chen, Z., Huang, H., Xu, Y., Tse, K.T., Kim, B., Wang, Y.: Unsteady aerodynamics
658 on a tapered prism under forced excitation. *Eng. Struct.* 240, 112387 (2021).
659 <https://doi.org/10.1016/j.engstruct.2021.112387>
- 660 22. Steckley, A., Vickery, B.J., Isyumov, N.: On the measurement of motion induced
661 forces on models in turbulent shear flow. *J. Wind Eng. Ind. Aerodyn.* 36, 339–350 (1990).
662 [https://doi.org/10.1016/0167-6105\(90\)90318-7](https://doi.org/10.1016/0167-6105(90)90318-7)
- 663 23. Vickery, B.J., Steckley, A.: Aerodynamic damping and vortex excitation on an
664 oscillating prism in turbulent shear flow. *J. Wind Eng. Ind. Aerodyn.* 49, 121–140 (1993).
665 [https://doi.org/10.1016/0167-6105\(93\)90009-D](https://doi.org/10.1016/0167-6105(93)90009-D)

- 666 24. Dai, H.L., Abdelmoula, H., Abdelkefi, A., Wang, L.: Towards control of cross-flow-
667 induced vibrations based on energy harvesting. *Nonlinear Dyn.* 88, 2329–2346 (2017).
668 <https://doi.org/10.1007/s11071-017-3380-x>
- 669 25. Abdel-Rohman, M.: Effect of Unsteady Wind Flow on Galloping of Tall Prismatic
670 Structures. 22
- 671 26. Dai, H.L., Abdelkefi, A., Wang, L., Liu, W.B.: Control of cross-flow-induced
672 vibrations of square cylinders using linear and nonlinear delayed feedbacks. *Nonlinear Dyn.*
673 78, 907–919 (2014). <https://doi.org/10.1007/s11071-014-1485-z>
- 674 27. Chen, X.: Estimation of stochastic crosswind response of wind-excited tall buildings
675 with nonlinear aerodynamic damping. *Eng. Struct.* 56, 766–778 (2013).
676 <https://doi.org/10.1016/j.engstruct.2013.05.044>
- 677
- 678
- 679